Characterisation, modelling and design of cut-off wavelength of InGaAs/GaAsSb Type-II Superlattice Photodiodes

To cite this article before publication: Jonathan Petticrew *et al* 2022 *Semicond. Sci. Technol.* in press https://doi.org/10.1088/1361-6641/aca8c9

IOP Publishing Journal Title
Journal **XX** (XXXX) XXXXXX https://doi.org/XXXX/XXXX

Characterisation, modelling and design of cut-off wavelength of InGaAs/GaAsSb Type-II Superlattice Photodiodes

Jonathan Petticrew[1], Yuting Ji[1], Im Sik Han[1], Benjamin White[2], Axel Evirgen[3], Jean-Luc Reverchon[3], Mark Hopkinson[1], Chee Hing Tan[1], and Jo Shien Ng[1]

1 Department of Electronic and Electrical Engineering, University of Sheffield, S1 3JD, United Kingdom.
2 Formally at 1. Now at Phlux Technology Ltd, S1 4DP, United Kingdom
3 III-V Lab, Palaiseau 91767, France

E-mail: j.s.ng@sheffield.ac.uk

Received xxxxxx
Accepted for publication xxxxxx
Published xxxxxx

Abstract

InGaAs/GaAsSb type-II superlattice (T2SL) photodiodes grown on InP substrates are an alternative detector technology for applications operating in the short wavelength infrared (SWIR) band. Their cut-off wavelengths are heavily influenced by the thickness and material composition of InGaAs and GaAsSb used in the T2SL. We present a single band k.p. model performed using a finite difference approach in nextnano validated against two T2SL photodiode wafers and results from literature. These photodiode wafers cover both lattice matched and strained $GaAs_{1-x}Sb_x$ compositions (x = 0.40, wafer A and 0.49, wafer B). The validation data covers temperature dependence of cut-off wavelengths (obtained from phase-sensitive photo response data) from 200 K to room temperature. The cut-off wavelengths were found to reduce at 1.32 nm/K for wafer A and 1.07 nm/K for wafer B. Good agreement was achieved between the validation data and nextnano simulations, after altering the $GaAs_{1-x}Sb_x$ valance band offset bowing parameter to -1.06 eV. Using this validated model, we show that the wavefunction overlap drops significantly if the GaAsSb barrier is thicker than the InGaAs well layer, hence defining the upper limit of the barrier layer. This validated model is then used to demonstrate that there is a linear dependence between the maximum achievable wavefunction overlap and cut-off wavelength of a lattice matched InGaAs/GaAsSb T2SL. We also found that the adoption of a 5 nm/3 nm InGaAs/GaAsSb T2SL structure offers an improved wavefunction overlap over the more common 5 nm/ 5 nm InGaAs/GaAsSb T2SL designs. The data reported in this paper is available from doi: 10.15131/shef.data.20310591.

Keywords: GaAsSb, Infrared detectors, InGaAs, Photodiodes, Superlattices, SWIR

1. Introduction

Detectors operating in the short wavelength infrared (SWIR) range (1-3 μm) have seen an increase in research focus due to several important applications covering the SWIR range. These include remote greenhouse gas monitoring [1], light detection and ranging (LiDAR) [2], and hyperspectral imaging [3].

There are several competing SWIR photodiode technologies, including HgCdTe [4], extended wavelength InGaAs (ex-InGaAs) [5], InAs [6], and InGaAs/GaAsSb superlattices. HgCdTe photodiodes are the most established, though also the most expensive, due to a combination of cryogenic operating temperatures (cooling engines are essential), highly specialized manufacturing technologies, and substrate cost (if using CdZnTe). Furthermore, the use of both Hg and Cd is being increasingly restricted.

Commercial ex-InGaAs photodiodes exhibit dark current densities approaching the 'Rule 07' benchmark for HgCdTe [4], [7]. However, due to the difference in lattice constants between ex-InGaAs materials and the InP substrates used, ex-InGaAs photodiodes contain misfit dislocations causing 1/*f* noise [5]. Ex-InGaAs photodiodes are also more susceptible to radiation damage compared to Si and InGaAs detectors [8]. InAs is a suitable SWIR material and InAs substrates are available commercially, but its cut-off wavelength (λ_c) of 3.55 μm is unnecessarily long for many SWIR applications.

InGaAs/GaAsSb Type-II superlattices (T2SL) can be grown on InP substrates using conventional III-V growth techniques. Their λ_c can be engineered by tailoring the superlattice well (InGaAs) and barrier (GaAsSb) thicknesses and compositions. Using InP substrates also facilitates two-colour photodiodes comprising of $In_{0.53}Ga_{0.47}As$ and T2SL sub-detectors [9].

Lattice-matched 5 nm/5 nm InGaAs/GaAsSb T2SL photodiodes exhibit λ_c of 2.4-2.5 μm at near room temperature [10], [11], responsivities of 0.47 - 1.4 A/W at 2.04 - 2.18 μm [10], [12], and bandwidths of 3.7 GHz [13]. To increase λ_c, some researchers used strain-compensated T2SL structures which apply compressive strain to the GaAsSb layers. For example, a 0.6% strain-compensation in a 5 nm/5 nm InGaAs/GaAsSb T2SL increases the room temperature λ_c from 2.6 to 2.8 μm [14]. Other researchers have explored recessed optical windows to increase quantum efficiency [15].

Commercial simulation software APSYS (from Crosslight Software Inc.) and nextnano have been used to simulate InGaAs/GaAsSb T2SL photodiodes [10], [11], [16]. The reported nextnano simulations were limited to a single lattice matched 5 nm/ 5 nm InGaAs/GaAsSb T2SL design and were performed using the default nextnano database values. These default values do not appear to be rigorously validated using experimental data. As will be shown later, T2SL simulation results of λ_c temperature dependence obtained using default values disagree with published data considerably.

In this work, we present a validated single-band k.p. model performed using a finite difference approach in nextnano for both strained and lattice-matched SWIR InGaAs/GaAsSb T2SL photodiodes. The validation data included experimental temperature dependence of λ_c from two SWIR T2SL photodiode wafers of this work and relevant reports in the literature. The validated model was then used to study the effects of GaAsSb composition on λ_c and wavefunction overlaps, using a 5 nm/3 nm T2SL design.

2. Characterisation

Two $In_{0.53}Ga_{0.47}As/GaAs_{1-x}Sb_x$ T2SL photodiode wafers were grown on n^+ InP substrates using molecular beam epitaxy (MBE) reactors equipped with As_2 and Sb_2 crackers and conventional In and Ga sources. Following the initial growth of an n-type $In_{0.53}Ga_{0.47}As$ layer, short periods of $In_{0.53}Ga_{0.47}As/GaAs_{1-x}Sb_x$ T2SL were grown. Growth interrupts were performed at each interface to allow sufficient time for the As_2 and Sb_2 sources to adjust to the required values. Growth was completed with $In_{0.53}Ga_{0.47}As$ and $In_{0.52}Al_{0.48}As$ layers at a raised substrate temperature. During wafer growth, two Ga cells were used to facilitate independent control of the $In_{0.53}Ga_{0.47}As$ and $GaAs_{1-x}Sb_x$ growth conditions.

Structure details of these wafers are summarized in Table 1. Wafer A contains lattice mismatched $GaAs_{1-x}Sb_x$ with x = 0.40, whereas wafer B is fully lattice matched (x = 0.49). Their T2SL periods and compositions were confirmed using theta-theta X-Ray diffraction (XRD) characteristics and transmission electron microscopy images. Fitting to the XRD data was performed using X-Ray Server [17]. XRD data and fitting (using structure details from Table 1) for wafer A are shown as an example in figure 1. There is good agreement in periodicity (fringe peak spacing) and overall shape.

Table 1. Structure details for wafers A and B

Material	Thickness (nm)	
	Wafer A	**Wafer B**
p^+ $In_{0.53}Ga_{0.47}As$	70	70
p^+ InAlAs	1000	1000
i- $In_{0.53}Ga_{0.47}As$	1000	1000
i- $In_{0.53}Ga_{0.47}As/GaAs_{1-x}Sb_x$ T2SL	5.5/3.0 x = 0.4 125 repeats	2.0/6.0 x = 0.49 250 repeats
n^+ $In_{0.53}Ga_{0.47}As$	800	200
n^+ InP Substrate		

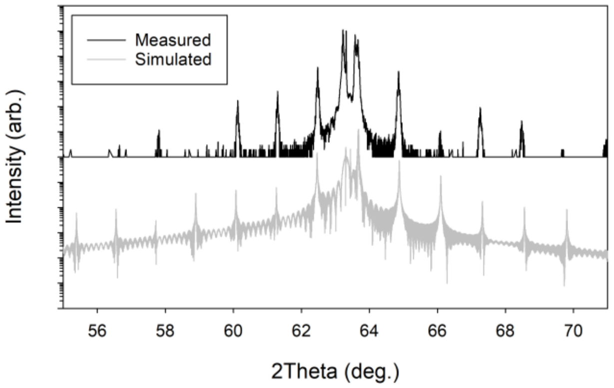

Figure 1. Experimental (top) 004 X-Ray diffraction characteristics and fitting (bottom) for wafer A.

Temperature dependent photocurrent versus wavelength measurements were carried out on the device-under-test (DUT) placed in a Janis ST-500 cryogenic probe station. A monochromator (using a grating with a 2.0 μm blaze wavelength) with a tungsten-halogen lamp provided the optical signal, which was mechanically chopped at 180 Hz before being delivered to the devices via optical fibres connected to the probe station. The end of the final optical fibre was positioned above the DUT's optical window. Phase-sensitive detection was employed (with a lock-in amplifier) to measure the resultant photocurrent flowing in the DUT in the presence of reverse dark current.

A commercial photodiode with a known responsivity versus wavelength characteristic was used to obtain the measurement system response, facilitating extraction of quantum efficiency (η) for the DUT. For each wafer and temperature, data were obtained from three same-sized devices. λ_c for a given temperature was extracted by linear regression fitting to the η^2 versus wavelength characteristics (from three devices), as shown in figure 2. From these linear regressions λ_c was defined where η^2 reaches zero. The temperature dependence of cut-off wavelengths were calculated as 1.32 and 1.07 nm/K for wafers A and B respectively, which are in broad agreement.

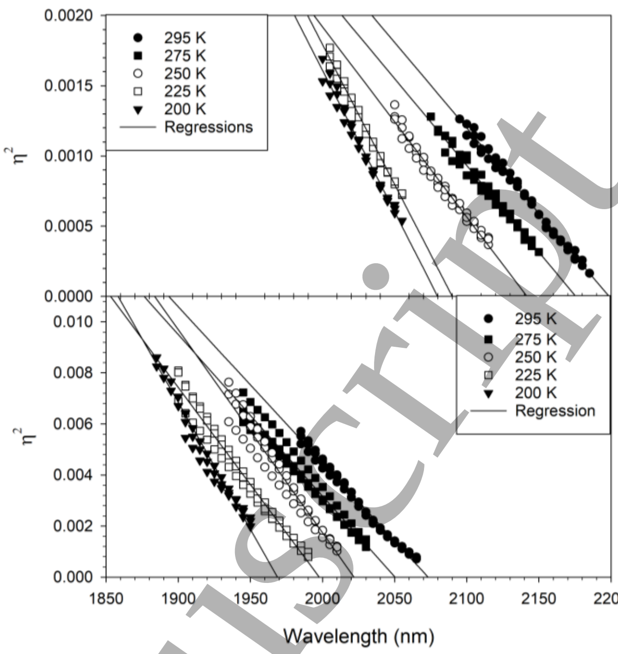

Figure 2. Extraction of λ_c using linear regression of η^2 for wafer A (top) and wafer B (bottom).

3. Modelling

Nextnano simulations were completed using single band k.p. theory through nextnano++. Temperature dependent bandgaps were included. The Varshni equation was used to calculate the temperature dependent bandgap of each composite binary. These were then interpolated to produce the ternary bandgaps. The full T2SL structure was included in the simulation, rather than relying on periodic boundary conditions. A grid spacing of 0.25 nm was used. Smaller grid spacing was tested, however there was little effect upon λ_c.

In the simulations, the device structure included a 20 nm thick InGaAs layer at either side of the T2SL region, instead of the entirety of the non-T2SL layers. Comparisons were made to confirm that this simplification does not affect the simulated values of λ_c. In addition, simulations of λ_c performed using nextnano++ versions 4.2.7.9 and 4.2.8.6, which yielded identical results.

Using the default parameter values, temperature dependence of λ_c for 5.0 nm/5.0 nm $In_{0.53}Ga_{0.47}As/GaAs_{0.51}Sb_{0.49}$ type-II superlattice were simulated. The results are compared to experimental reports from [10] and [12] in figure 3a. There is a large discrepancy of ~0.6 μm across the temperature range covered.

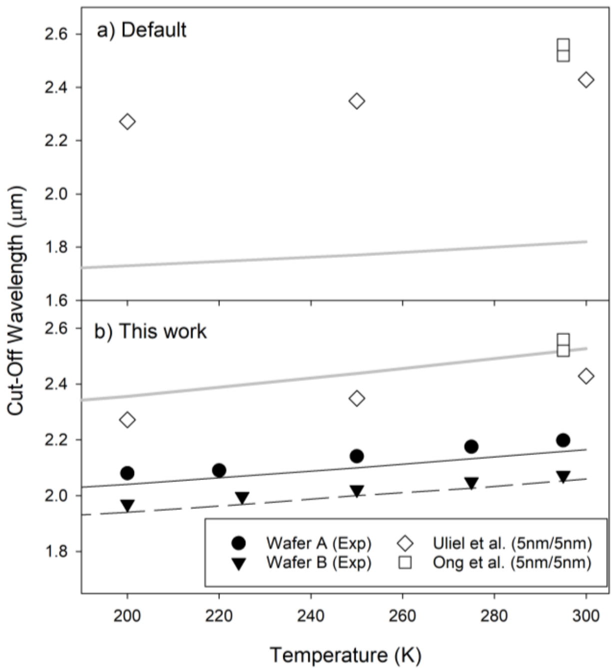

Figure 3. Comparison between simulated (lines) and experimental (symbols: diamonds [10] and squares [12]) λ_c for a) a 5 nm/5 nm InGaAs/GaAsSb type-II superlattice using the nextnano default parameters and b) a 5 nm/5 nm InGaAs/GaAsSb type-II superlattice and wafers from this work using a $GaAs_{1-x}Sb_x$ valence band offset bowing parameter of -1.06 eV.

Since λ_c values from T2SL structures are heavily influenced by the valance band offset (VBO) between the two constituent materials, the discrepancy between experimental and simulated results was minimised by correcting the VBO. Rather than having to calculate the VBOs between every combination of materials nextnano takes a different, simpler, approach. Each material has a VBO calculated independently on an absolute scale, often referenced against InSb [18]. These independently calculated absolute VBOs can then be used to align any combination of materials. Changing these absolute VBO values has no effect on the bulk bandgaps of the individual materials (e.g. InGaAs).

For GaAsSb this absolute VBO is calculated by bowing between the absolute VBOs of GaAs and GaSb. Replacing the GaAsSb VBO bowing parameter (from its default value of 0 eV) with -1.06 eV [18], good agreement was achieved for the simulation and experimental values from figure 2, as shown in figure 3b. The experimental values, which are the validation data of this work, include those from the 5.0 nm/5.0 nm $In_{0.53}Ga_{0.47}As/GaAs_{0.51}Sb_{0.49}$ T2SL ([10] and [12]) as well as our data from wafers A and B. The discrepancy in results between [10] and [12] are thought to be due to the Zn-diffusion process undergone in [10], which noted additional XRD satellite peaks post-diffusion. Note that the data from [10], [12] and wafer B group are lattice-matched T2SL whereas wafer A is a strained T2SL. Hence our validated model for temperature dependence of λ_c is valid for both strained and lattice matched T2SL structures. A detailed set of parameter values used in our model is provided in the data repository [19].

4. Design

Having obtained the experimental data that was used to achieve a validated model, we explore a series of T2SL designs. For each design we calculated the wavefunction overlap (given by the overlap between the square modulus of the electron and hole wavefunctions), which is important for interband optical transitions.

A series of room temperature λ_c simulations were carried out for lattice matched T2SL designs with $In_{0.53}Ga_{0.47}As$ thickness of 3 to 7 nm and $GaAs_{0.51}Sb_{0.49}$ thickness of 2 nm to 9 nm. The simulated λ_c versus wavefunction overlap characteristics are plotted in figure 4 (top). For a given $In_{0.53}Ga_{0.47}As$ thickness, increasing the thickness of the GaAsSb increases λ_c. However, this is at the expense of reduced wavefunction overlap and thus photon absorption efficiency.

In figure 4 (top), we can observe a rapid decrease in wavefunction overlap with barrier thickness, when the barrier becomes thicker than the well, placing an upper limit for practical barrier thicknesses. Furthermore, using the largest wavefunction overlap values for a given λ_c, there is an empirical linear relationship between wavefunction overlap and λ_c the upper SWIR band of,

$$W = 76.8 - m\lambda,$$

where W and λ represent the wavefunction overlap and cut-off wavelength in µm and m has a value of 26.0 %.µm^{-1}, as shown in figure 4 (bottom).

Another approach to change the cut-off wavelength is by changing the composition of the well or barrier, e.g. in ref [16]. To explore the effect of the $GaAs_{1-x}Sb_x$ composition on λ_c, a further set of simulations were carried out using the 5 nm/3 nm InGaAs/GaAsSb T2SL designs. With $GaAs_{1-x}Sb_x$ compositions between x = 0.3 and 0.6, the T2SL λ_c values can cover the entire SWIR range, as shown in figure 5.

Using simulation results from figure 5 and ref [16], the dependence of λ_c values on $GaAs_{1-x}Sb_x$ composition is summarised in Table 2 for 5 nm/3 nm and 5 nm/5 nm T2SL designs. The λ_c from 5 nm/3 nm T2SL design is slightly more sensitive to changes in $GaAs_{1-x}Sb_x$ composition, compared to its 5 nm/5 nm counterpart. However, the 5 nm/3 nm design offers an improved wavefunction overlap at a given λ_c. This suggests that asymmetric T2SL structures with a thinner barrier offer higher photon absorption efficiency, however their λ_c are more sensitive to $GaAs_{1-x}Sb_x$ composition variation in wafer growths.

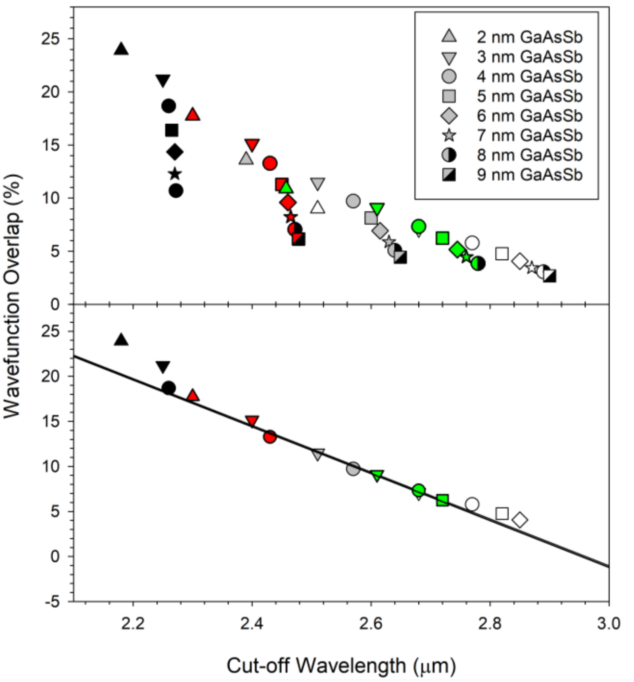

Figure 4. (Top) Simulated wavefunction overlap of lattice matched InGaAs/GaAsSb type-II superlattice with InGaAs thickness of 3 (black), 4 (red), 5 (grey), 6 (green), and 7 nm (white). (Bottom) Empirical linear relationship of maximum wavefunction overlap against cut-off wavelength.

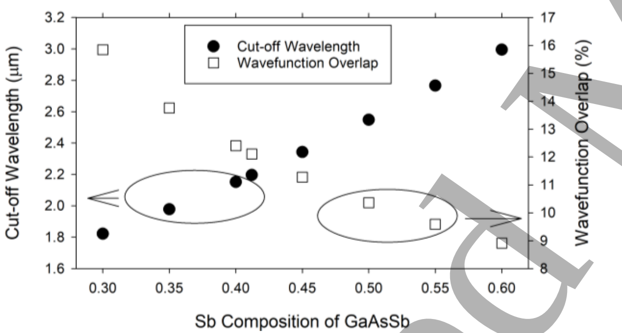

Figure 5. Simulated room temperature λ_c (left, circles) and wavefunction overlap (right, squares) for a 5 nm/3 nm strained InGaAs/GaAsSb type-II superlattice with 125 periods for different GaAsSb compositions.

Table 2. Comparison between 5nm/3nm and 5nm/5nm InGaAs/GaAsSb type-II superlattices. * indicates lattice matched GaAsSb

Structure	$GaAs_{1-x}Sb_x$ composition	λ_c (μm)	Wavefunction overlap (%)
5nm/3nm (this work)	x = 0.49*	2.5	11.5
	x = 0.57	2.8	10.5
	x = 0.60	3.0	8.9
5nm/5nm [14]	x = 0.49*	2.4	10.4
	x = 0.60	2.8	8.0

5. Conclusion

Two asymmetric InGaAs/GaAsSb T2SL have been grown by MBE. These wafers contained strained and lattice matched $GaAs_{1-x}Sb_x$ (x = 0.49 and 0.40). Temperature dependence of cut-off wavelength was extracted from phase-sensitive photoresponse data between 200 K and room temperature. These results along with literature were then used to validate a single-band k.p. model for temperature dependent T2SL.

Using this validated model, we show a significant drop in wavefunction overlap if the GaAsSb barrier is thicker than the InGaAs well placing an upper limit on barrier thickness. This model also suggests a linear relationship between maximum achievable wavefunction overlap and cut-off wavelength for lattice matched InGaAs/GaAsSb T2SL.

Advantages of the 5 nm/3 nm InGaAs/GaAsSb T2SL was then explored. Adopting the 5 nm/3 nm structure over a more common 5 nm/ 5 nm structure offers higher wavefunction overlap, which will benefit absorption efficiency. However, the 5 nm/3 nm structure's cut-off wavelength is more sensitive to variation in the Sb composition of $GaAs_{1-x}Sb_x$.

6. Acknowledgements

This work was supported by the EU H2020 program "SWIRup" (grant agreement 776278).

References

[1] Ehret G., Bousquet P., Pierangelo C., Alpers M., Millet B., Abshire J. B., Bovensmann H., Burrows J. P., Chevallier F., Ciais P., Crevoisier C., Fix A., Flamant P., Frankenberg C., Gibert F., Heim B., Heimann M., Houweling S., Hubberten H., Jöckel P., Law K., Löw A., Marshall J., Agusti-Panareda A., Payan S., Prigent C., Rairoux P., Sachs T., Scholze M., and Wirth M., "MERLIN: A French-German Space Lidar Mission Dedicated to Atmospheric Methane," *Remote Sens.*, vol. 9, no. 10, p. 1052, Oct. 2017. Doi: 10.3390/rs9101052

[2] Royo S. and Ballesta-Garcia M., "An Overview of Lidar Imaging Systems for Autonomous Vehicles", *Appl. Sci.*, vol. 9, no. 19, 4093, Sept. 2019. Doi: 10.3390/app9194093

[3] Tan K., Wang H., Chen L., Du Q., Du P., and Pan C., "Estimation of the spatial distribution of heavy metal in agricultural soils using airborne hyperspectral imaging and random forest," *J. Hazard. Mater.*, vol. 382, p. 120987, Jan. 2020, doi: 10.1016/j.jhazmat.2019.120987.

[4] Yuan H., Zhang J., Kim J., Bond D., Laquindanum J., Kimchi J., and DeForest M.G., "Recent progress in extended wavelength InGaAs photodetectors and comparison with SWIR HgCdTe photodetectors," in *Proc. SPIE 11129*, Sep. 2019, p. 11, doi: 10.1117/12.2532418.

[5] Ma Y., Li X., Shao X., Deng S., Cheng J., Gu Y., Liu Y., Y. Chen Y., Zhu X., Li T., Zhang Y., Gong H., and Fang J. "320×256 Extended Wavelength InxGa1-xAs/InP Focal Plane Arrays: Dislocation Defect, Dark Signal and Noise," *IEEE J. Select. Topics Quantum Electron.*, vol. 28, no. 2, pp. 1–11, Mar. 2022, doi: 10.1109/JSTQE.2021.3087182.

[6] Zhou X., Meng X., Krysa A. B., Willmott J. R., Ng J. S., and Tan C. H., "InAs Photodiodes for 3.43 micron Radiation Thermometry," *IEEE Sens. J.*, vol. 15, no. 10, pp. 5555–5560, Oct. 2015, doi: 10.1109/JSEN.2015.2443563.

[7] Tennant W. E., Lee D., Zandian M., Piquette E., and Carmody M., "MBE HgCdTe Technology: A Very General Solution to IR Detection, Described by 'Rule 07', a Very Convenient Heuristic," *J. Electron. Mater.*, vol. 37, no. 9, pp. 1406–1410, Sep. 2008, doi: 10.1007/s11664-008-0426-3.

[8] Kleipool Q. L., Jongma R. T., Gloudemans A. M. S., Schrijver H., Lictenberg G. F., van Hees R. M., Maurellis A. N., and Hoogeveen R. W. M., "In-flight proton-induced radiation damage to SCIAMACHY's extended-wavelength InGaAs near-infrared detectors," *Infrared Phys. Technol.*, vol. 50, no. 1, pp. 30–37, Mar. 2007, doi: 10.1016/j.infrared.2006.08.001.

[9] Xie Z., Deng Z., Zou X., and Chen B., 'InP-Based Near Infrared/Extended-Short Wave Infrared Dual-Band Photodetector', *IEEE Photon. Technol. Lett.*, vol. 32, no. 16, pp. 1003–1006, Aug. 2020, doi: 10.1109/LPT.2020.3008853

[10] Uliel Y., Cohen-Elias D., Sicron N., Grimberg I., Snapi N., Paltiel Y., and Katz M., 'InGaAs/GaAsSb Type-II superlattice based photodiodes for short wave infrared detection', *Infrared Phys. Technol.*, vol. 84, pp. 63–71, Aug. 2017, doi: 10.1016/j.infrared.2017.02.003.

[11] Easley J., Martin C. R., Ettenberg M. H., and Phillips J., 'InGaAs/GaAsSb Type-II Superlattices for Short-Wavelength Infrared Detection', *J. Electron. Mater.*, vol. 48, no. 10, pp. 6025–6029, Oct. 2019, doi: 10.1007/s11664-019-07441-x.

[12] Ong D. S. G., Ng J. S., Goh Y. L., Tan C. H., Zhang S., and David J. P. R., 'InAlAs Avalanche Photodiode With Type-II Superlattice Absorber for Detection Beyond 2μm', *IEEE Trans. Electron Devices*, vol. 58, no. 2, pp. 486–489, Feb. 2011, doi: 10.1109/TED.2010.2090352.

[13] Chen Y., Zhao X., Huang J., Deng Z., Cao C., Gong Q., and Chen B., "Dynamic model and bandwidth characterization of InGaAs/GaAsSb type-II quantum wells PIN photodiodes", *Opt. Express*, vol. 26, no. 26, pp. 35034-35045, Dec 2018, doi: 10.1364/OE.26.035034.

[14] Yonezawa Y., Hiraike R., Miura K., Iguchi Y., and Kawamura Y., "Growth and characterization of strain-compensated InGaAs/GaAsSb type II multiple quantum wells on InP substrate," *Physica E Low Dimens. Syst. Nanostruct.*, vol. 42, no. 10, pp. 2781–2783, Sep. 2010, doi: 10.1016/j.physe.2009.12.030.

[15] Wang J., Xie Z, Zhu L., Zou X., Zhou X., Yu W., Liu R., Du A., Gong Q., and Chen B., "InP-based broadband photodetectors with InGaAs/GaAsSb Type-II superlattices", *IEEE Electron. Device Lett.*, vol. 43, no. 5, pp. 757-760, May 2022, doi: 10.1109/LED.2022.3162246

[16] Chen B., Jiang W. Y., and Holmes A. L., "Design of strain compensated InGaAs/GaAsSb type-II quantum well structures for mid-infrared photodiodes," *Opt. Quantum Electron.*, vol. 44, no. 3, pp. 103–109, Jun. 2012, doi: 10.1007/s11082-011-9524-1.

[17] Stepanov S., "X-ray server: an online resource for simulations of X-ray diffraction and scattering". in *Proc. SPIE 5536*, 2004, p.16-26. doi: 10.1117/12.557549

[18] Vurgaftman I., Meyer J. R., and Ram-Mohan L. R., "Band parameters for III–V compound semiconductors and their alloys," *J. Appl. Phys.*, vol. 89, no. 11, pp. 5815–5875, Jun. 2001, doi: 10.1063/1.1368156.

[19] Petticrew J., Ji Y., Han I.S., White B. Axel E., Reverchon R.-L., Hopkinson M., Tan C.H., Ng J.S., "Data for paper: Characterisation, modelling and design of cut-off wavelength of InGaAs/GaAsSb Type-II Superlattice Photodiodes". The University of Sheffield. Dataset. doi: 10.15131/shef.data.20310591